

## Article

# Ag Decoration and SnO<sub>2</sub> Coupling Modified Anatase/Rutile Mixed Crystal TiO<sub>2</sub> Composite Photocatalyst for Enhancement of Photocatalytic Degradation towards Tetracycline Hydrochloride

Mao Tang<sup>1,2</sup>, Yangwen Xia<sup>1</sup>, Daixiong Yang<sup>1</sup>, Shiji Lu<sup>1</sup>, Xiaodong Zhu<sup>1,2,\*</sup> , Renyong Tang<sup>3</sup> and Wanming Zhang<sup>4,\*</sup>

<sup>1</sup> School of Mechanical Engineering, Chengdu University, Chengdu 610106, China; tangmao@cdu.edu.cn (M.T.); x1278704108@163.com (Y.X.); yangdaixiong1998@163.com (D.Y.); l3221668248@163.com (S.L.)

<sup>2</sup> Sichuan Province Engineering Technology Research Center of Powder Metallurgy, Chengdu 610106, China

<sup>3</sup> School of Food and Biological Engineering, Chengdu University, Chengdu 610106, China; tangrenyong@cdu.edu.cn

<sup>4</sup> School of Resources and Environment, Xichang University, Xichang 615000, China

\* Correspondence: zhuxiaodong@cdu.edu.cn (X.Z.); zhangwanming@xcc.edu.cn (W.Z.)

**Abstract:** The anatase/rutile mixed crystal TiO<sub>2</sub> was prepared and modified with Ag decoration and SnO<sub>2</sub> coupling to construct a Ag@SnO<sub>2</sub>/anatase/rutile composite photocatalytic material. The crystal structure, morphology, element valence, optical properties and surface area were characterized, and the effects of Ag decoration and SnO<sub>2</sub> coupling on the structure and photocatalytic properties of TiO<sub>2</sub> were studied. Ag decoration and SnO<sub>2</sub> coupling are beneficial to reduce the recombination of photogenerated electrons and holes. When the two modification are combined, a synergistic effect is produced in suppressing the photogenerated charge recombination, making Ag@SnO<sub>2</sub>/TiO<sub>2</sub> exhibits the highest quantum utilization. After 30 min of illumination, the degradation degree of tetracycline hydrochloride (TC) by pure TiO<sub>2</sub> increased from 63.3% to 83.1% with Ag@SnO<sub>2</sub>/TiO<sub>2</sub>.

**Keywords:** anatase/rutile mixed crystal TiO<sub>2</sub>; Ag decoration; SnO<sub>2</sub> coupling; photocatalytic activity; tetracycline hydrochloride



**Citation:** Tang, M.; Xia, Y.; Yang, D.; Lu, S.; Zhu, X.; Tang, R.; Zhang, W. Ag Decoration and SnO<sub>2</sub> Coupling Modified Anatase/Rutile Mixed Crystal TiO<sub>2</sub> Composite Photocatalyst for Enhancement of Photocatalytic Degradation towards Tetracycline Hydrochloride. *Nanomaterials* **2022**, *12*, 873. <https://doi.org/10.3390/nano12050873>

Academic Editor:  
Diego Cazorla-Amorós

Received: 28 January 2022

Accepted: 2 March 2022

Published: 6 March 2022

**Publisher's Note:** MDPI stays neutral with regard to jurisdictional claims in published maps and institutional affiliations.



**Copyright:** © 2022 by the authors. Licensee MDPI, Basel, Switzerland. This article is an open access article distributed under the terms and conditions of the Creative Commons Attribution (CC BY) license (<https://creativecommons.org/licenses/by/4.0/>).

## 1. Introduction

Antibiotics have been widely used in our daily life for decades. If they are not treated as non-toxic, these antibiotics will eventually enter the water and soil, threatening human health [1–4]. Employing photocatalytic technology to degrade antibiotics is a green and efficient route, which shows broad application prospects. Among various photocatalytic materials, TiO<sub>2</sub>-based photocatalysts have received the most attention in the degradation of antibiotics [5–7].

However, due to the low utilization of sunlight and the high recombination rate of photogenerated electrons and holes of pure TiO<sub>2</sub>, it is necessary to modify its energy band structure and improve the visible light utilization and quantum efficiency to increase the photocatalytic activity [8–10]. When TiO<sub>2</sub> particles contact with precious metal, forming heterojunctions, the photogenerated electrons on the conduction band of TiO<sub>2</sub> will migrate to the precious metal particles until the Fermi energy level is equal, which enhances the separation photogenerated charges [11–13]. In the research of noble metal decoration, Ag has attracted extensive attention because of its relatively cheap and excellent modification effects [14–18].

Li et al. [15] fabricated Ag nanoparticle-decorated porous TiO<sub>2</sub> foams using the wet-impregnation method. Due to the surface plasmon resonance (SPR) effect of Ag nanoparticles, the absorption in visible light was greatly enhanced, and thus the photocatalytic

performance of TiO<sub>2</sub> was improved. In other modification methods, TiO<sub>2</sub> coupling with else semiconductors promotes the migration of photogenerated charges at the two-phase interface, thus, increasing the quantum utilization and photocatalytic efficiency [19,20]. SnO<sub>2</sub>/TiO<sub>2</sub> semiconductor systems have been widely studied as the band position of SnO<sub>2</sub> matches TiO<sub>2</sub>.

When TiO<sub>2</sub> is illuminated, photogenerated holes and photogenerated electrons are generated in the valence band and conduction band, respectively. The electrons will transfer to the conduction band of SnO<sub>2</sub>, and the holes in the SnO<sub>2</sub> valence band will migrate to TiO<sub>2</sub> valence band, which separates the photogenerated electrons and holes effectively. Therefore, SnO<sub>2</sub>/TiO<sub>2</sub> exhibits better photocatalytic performance compared with pure TiO<sub>2</sub> [21–23]. Xun et al. introduced SnO<sub>2</sub> into TiO<sub>2</sub> nanotube materials to improve the quantum efficiency and obtained a higher photocatalytic activity [22].

In addition to coupling with other semiconductor materials, TiO<sub>2</sub> with different crystal structures to form mix crystal heterojunctions is also conducive to the transfer of photogenerated charges, showing higher photocatalytic activity than a single crystal structure [24–26]. Based on these advantages, anatase/rutile mixed crystal TiO<sub>2</sub> was prepared by the sol-gel method and modified by Ag decoration and SnO<sub>2</sub> coupling to fabricate Ag@SnO<sub>2</sub>/anatase/rutile composite photocatalyst in the present work.

The crystal structure, morphology, element valence, optical properties and surface area were characterized. The photocatalytic performance of the prepared photocatalysts was assessed by taking tetracycline hydrochloride aqueous solution as the target pollutant. The effects of Ag decoration and SnO<sub>2</sub> coupling on the structure and photocatalytic performance of mixed crystal TiO<sub>2</sub> were investigated in detail.

## 2. Experimental Section

### 2.1. Material Preparation

Butyl titanate (Analytical Reagent, AR), absolute ethanol (AR), hydrochloric acid (AR), tin tetrachloride pentahydrate (AR), silver nitrate (AR), tetracycline hydrochloride (AR), benzoquinone (AR), ammonium oxalate (AR) and isopropanol (AR) were purchased from Chengdu Chron Chemicals Co., Ltd., (Chengdu, China).

We added 20 mL butyl titanate and 45 mL absolute ethanol to a beaker to form mixture A. We mixed 10 mL deionized water, 15 mL absolute ethanol and 2 mL hydrochloric acid to obtain mixture B, which was added into mixture A dropwise to form a gel. After aging and drying, the powder was calcined at 550 °C for 1 h to prepare pure TiO<sub>2</sub>.

Silver nitrate (AgNO<sub>3</sub>) or tin tetrachloride pentahydrate (SnCl<sub>4</sub>·5H<sub>2</sub>O) was added into mixture B. Keep the other steps unchanged to fabricate Ag decorated TiO<sub>2</sub> and SnO<sub>2</sub> coupled TiO<sub>2</sub>, which are labelled as Ag@TiO<sub>2</sub> and SnO<sub>2</sub>/TiO<sub>2</sub>. The molar ratios of Ag:Ti and Sn:Ti were 1:100 and 75:100, separately. When AgNO<sub>3</sub> and SnCl<sub>4</sub>·5H<sub>2</sub>O were added simultaneously, the Ag@SnO<sub>2</sub>/TiO<sub>2</sub> composite photocatalyst was obtained.

### 2.2. Characterization

The crystal structure was analyzed using a DX-2700 X-ray diffractometer (Dandong Haoyuan Instrument Co. Ltd., Dandong, China, XRD). The test voltage was 40 kV, the current was 30 mA, and the scanning angle was 20°–70° with the scanning speed 0.06° /s. The morphology (SEM and TEM) was observed using a FEI-Inspect F50 scanning electron microscope and a FEI-Tecna G2 F20 transmission electron microscope (FEI Company, Hillsboro, OR, USA). Adopting an XSAM800 multifunctional surface analysis system to study the element composition and valence state (XSAM800, Kratos Ltd., Manchester, Britain, XPS). The recombination of photo-induced charges was analyzed by a F-4600 fluorescence spectrometer (F-4600, Shimadzu Group Company, Kyoto, Japan, PL). The optical absorption was tested by a UV-3600 UV-Vis spectrophotometer (UV-3600, Shimadzu Group Company, Kyoto, Japan, DRS). The BET specific surface area was analyzed by a Mike ASAP2460 analyzer (Mike Instrument Company, Atlanta, GA, USA).

### 2.3. Photocatalysis Experiment

Tetracycline hydrochloride (TC) was employed as the target pollutant to evaluate the photocatalytic performance. We added 100 mL (30 mg/L) TC aqueous solution and 0.1 g sample to a beaker and stirred for 30 min in dark. Then, a 250 W xenon lamp (Solar-350, Beijing NBeT Technology Co. Ltd., Beijing, China) was turned on as the light source for irradiation. The mixture was taken every 10 min and extracted after centrifugation, and the absorbance ( $A$ ) of the supernatant at 355 nm was measured by an ultraviolet visible spectrophotometer. The degradation degree was computed by the formula as follows:

$$(A_0 - A_t)/A_0 \times 100\% \quad (1)$$

## 3. Results and Discussion

### 3.1. XRD Analysis

The XRD patterns of samples are shown in Figure 1. In the pattern of pure  $\text{TiO}_2$ , the peaks at  $25.3^\circ$ ,  $37.9^\circ$  and  $48.1^\circ$  correspond to the (101), (004) and (200) crystal planes of anatase, and the peaks at  $27.4^\circ$ ,  $36.1^\circ$  and  $54.3^\circ$  are indexed to the (110), (101) and (211) crystal planes of rutile, indicating that pure  $\text{TiO}_2$  consists of anatase and rutile and shows mixed crystal structure [24,26–28]. The mass fractions of anatase and rutile are 23.8% and 76.2%, respectively.

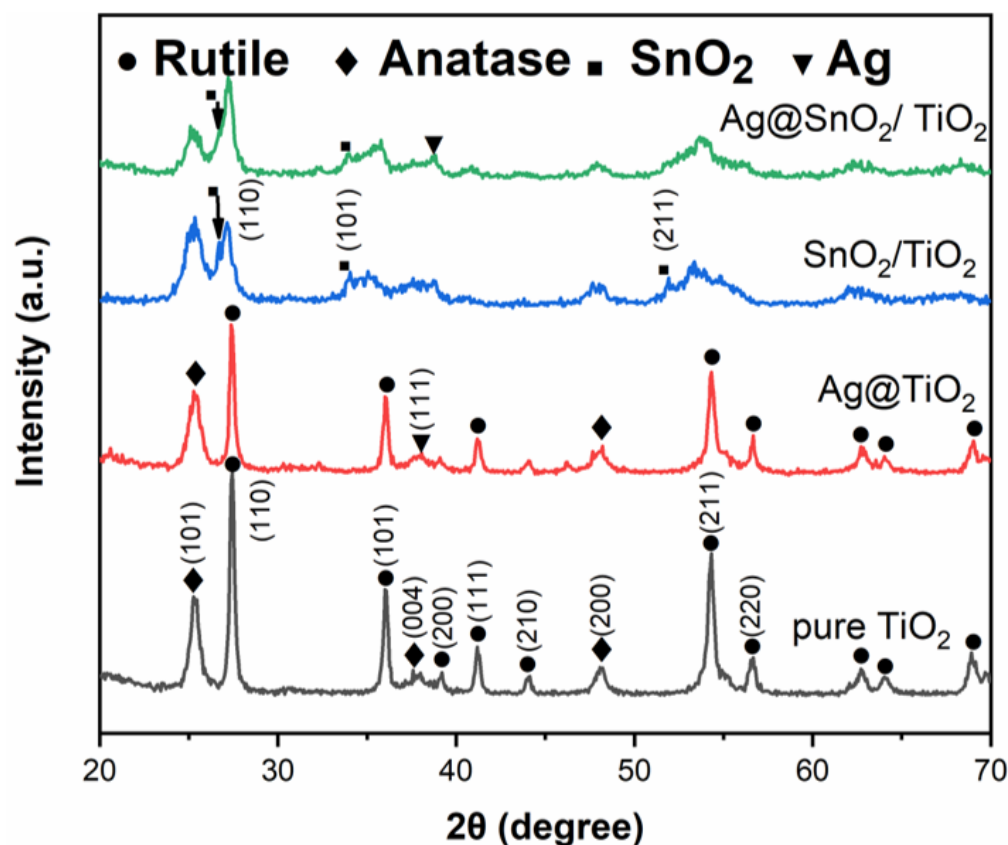
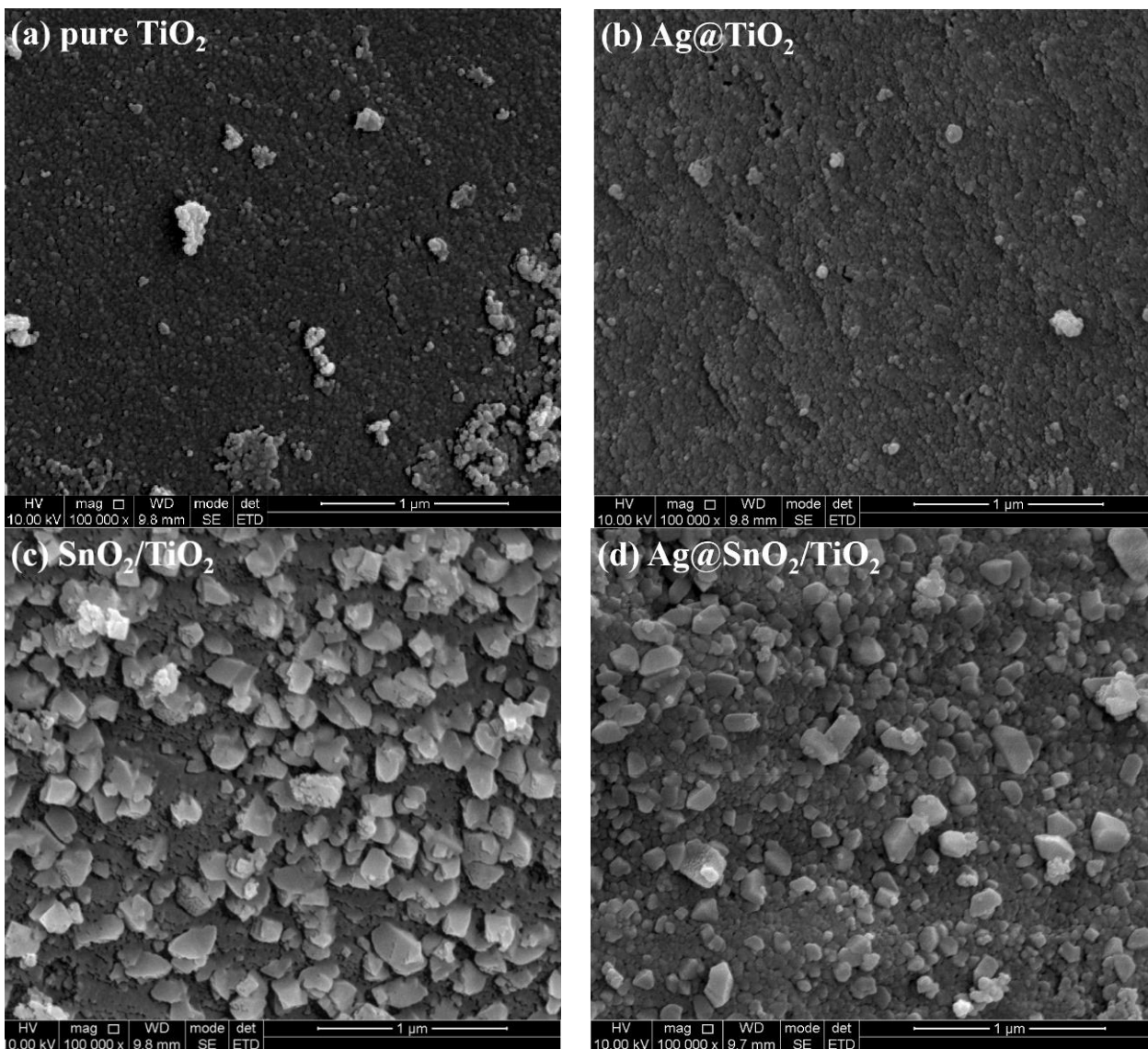


**Figure 1.** XRD patterns of pure  $\text{TiO}_2$ ,  $\text{Ag@TiO}_2$ ,  $\text{SnO}_2/\text{TiO}_2$  and  $\text{Ag@SnO}_2/\text{TiO}_2$ .

In the pattern of  $\text{Ag@TiO}_2$ , in addition to the anatase and rutile peaks, the peak appearing at  $38.1^\circ$  corresponds to the (111) crystal plane of elemental Ag [29], which implies that  $\text{Ag@TiO}_2$  heterojunctions are formed. The peaks at  $26.7^\circ$ ,  $34.0^\circ$  and  $51.9^\circ$  in the patterns of  $\text{SnO}_2/\text{TiO}_2$  are indexed to the (110), (101), (211) crystal planes of  $\text{SnO}_2$  [30], showing that  $\text{SnO}_2/\text{TiO}_2$  semiconductor composites are generated. The diffraction peaks of  $\text{SnO}_2$  and Ag appear in the pattern of  $\text{Ag@SnO}_2/\text{TiO}_2$ , which shows that the  $\text{Ag@SnO}_2/\text{TiO}_2$  composite photocatalyst was constructed through Ag decoration and  $\text{SnO}_2$  coupling.

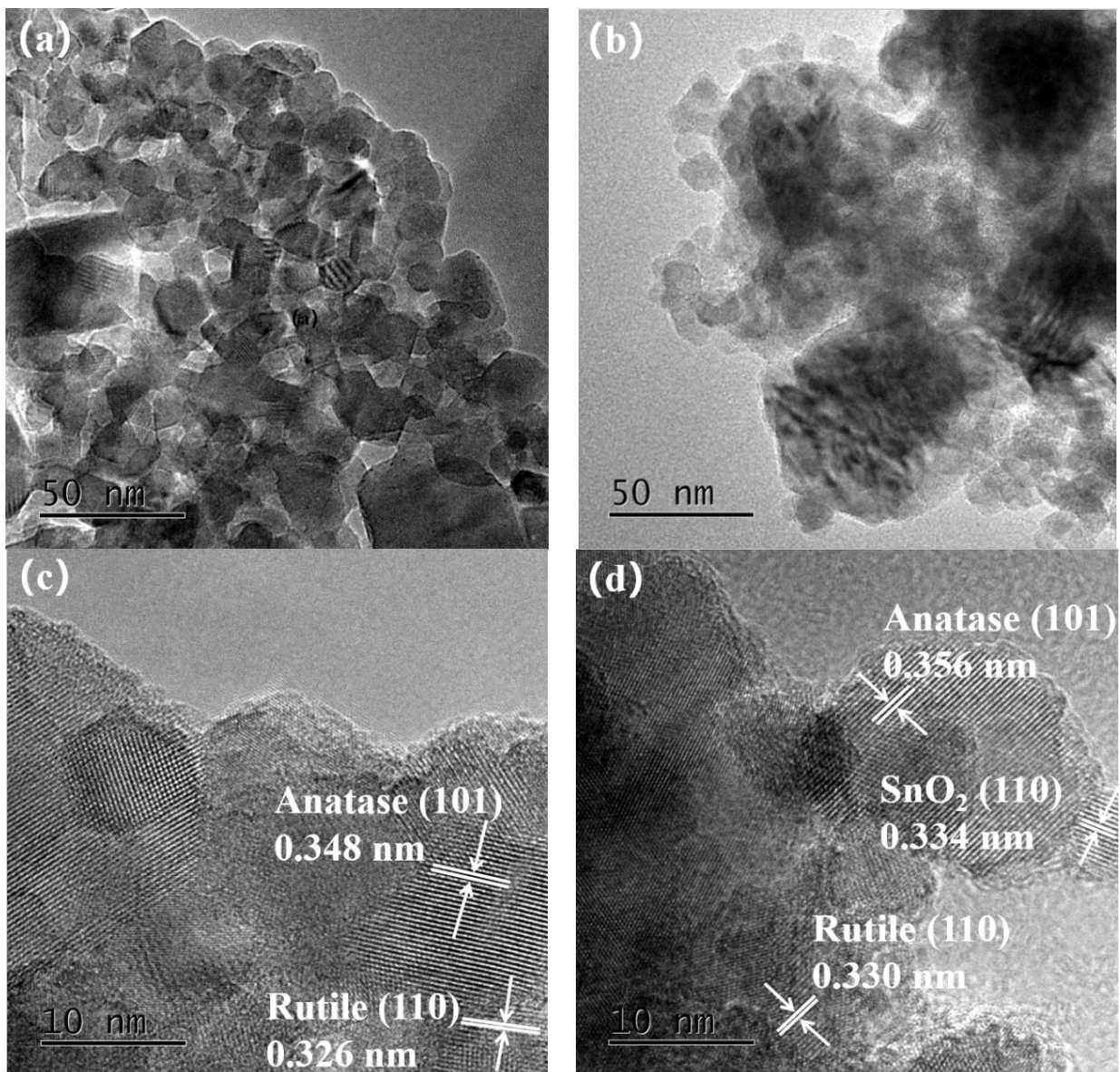
### 3.2. SEM and TEM Analyses

Figure 2 depicts the SEM images of pure  $\text{TiO}_2$ ,  $\text{Ag@TiO}_2$ ,  $\text{SnO}_2/\text{TiO}_2$  and  $\text{Ag@SnO}_2/\text{TiO}_2$ . Pure  $\text{TiO}_2$  presents a granular morphology with several agglomerates.  $\text{Ag@TiO}_2$  shows a similar morphology to pure  $\text{TiO}_2$ . The particle size increases in  $\text{SnO}_2/\text{TiO}_2$  and  $\text{Ag@SnO}_2/\text{TiO}_2$  samples.



**Figure 2.** SEM images of pure  $\text{TiO}_2$  (a),  $\text{Ag@TiO}_2$  (b),  $\text{SnO}_2/\text{TiO}_2$  (c) and  $\text{Ag@SnO}_2/\text{TiO}_2$  (d).

Figure 3 presents the TEM and HRTEM images of pure  $\text{TiO}_2$  (Figure 3a,c) and  $\text{Ag@SnO}_2/\text{TiO}_2$  (Figure 3b,d). It is observed in Figure 3a that the particle size of pure  $\text{TiO}_2$  is about 20–30 nm. In Figure 3c, the marked interplanar spacing 0.348 nm corresponds to the anatase (101) crystal plane, and 0.326 nm corresponds to the rutile (110) crystal plane [7,31,32], indicating that pure  $\text{TiO}_2$  is composed of anatase and rutile and exhibits a mixed crystal structure. The particle size in Figure 3b is slightly smaller than pure  $\text{TiO}_2$ , which is in the range of 15–20 nm.



**Figure 3.** TEM and HRTEM images of pure  $\text{TiO}_2$  (a,c) and  $\text{Ag@SnO}_2/\text{TiO}_2$  (b,d).

The interplanar spacing 0.356 nm in Figure 3d corresponds to the anatase (101) crystal plane, which is larger than that of pure  $\text{TiO}_2$  (0.348 nm). As the radius of  $\text{Sn}^{4+}$  (0.0690 nm) is larger than that of  $\text{Ti}^{4+}$  (0.0605 nm), the replacement of  $\text{Ti}^{4+}$  by  $\text{Sn}^{4+}$  will cause a lattice expansion, resulting in the increase of interplanar spacing [33]. The marked interplanar spacing 0.330 nm corresponds to the rutile (110) crystal plane [34]. The interplanar spacing 0.334 nm can be attributed to the (110) crystal plane of  $\text{SnO}_2$  [35].

### 3.3. XPS Analysis

The XPS results of pure  $\text{TiO}_2$  and  $\text{Ag@SnO}_2/\text{TiO}_2$  are shown in Figure 4. Figure 4a shows the full spectra. The constituent elements of  $\text{Ag@SnO}_2/\text{TiO}_2$  are Ti, O, Sn, Ag and C. The signal of C element mainly comes from the pollution during the test. Figure 4b is the high-resolution spectra of Ti 2p. The binding energies of  $\text{Ti}^{4+}$  2p<sub>3/2</sub> and  $\text{Ti}^{4+}$  2p<sub>1/2</sub> are 458.5 and 464.1 eV, indicating that Ti element is +4 valence in pure  $\text{TiO}_2$  [36]. The  $\text{Ti}^{4+}$  2p<sub>3/2</sub> and  $\text{Ti}^{4+}$  2p<sub>1/2</sub> binding energies of  $\text{Ag@SnO}_2/\text{TiO}_2$  shifts to higher binding energies, which are at 459.3 and 465.0 eV.

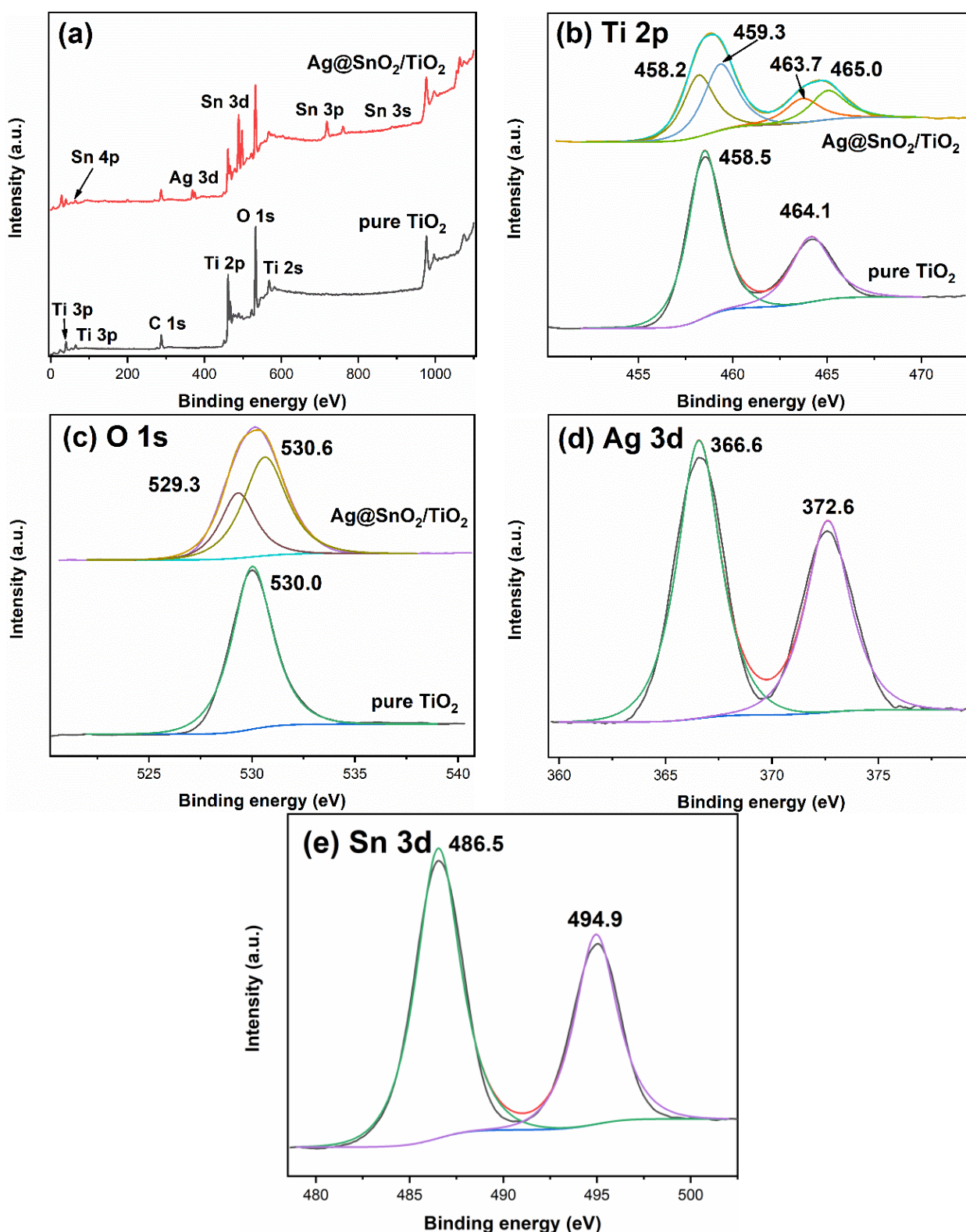


**Figure 4.** XPS spectra of pure TiO<sub>2</sub> and Ag@SnO<sub>2</sub>/TiO<sub>2</sub>: total spectra (a), Ti 2p (b), O 1s (c), Ag 3d (d) and Sn 3d (e).

In addition, characteristic peaks at 458.2 and 463.7 eV corresponding to Ti<sup>3+</sup> 2p<sub>1/2</sub> and Ti<sup>3+</sup> 2p<sub>3/2</sub> appear, indicating that Ti exists as +3 and +4 in Ag@SnO<sub>2</sub>/TiO<sub>2</sub> [37]. Figure 4c shows the O 1s high-resolution spectra. Pure TiO<sub>2</sub> shows a characteristic peak at 530.0 eV, which corresponds to lattice oxygen (O<sup>2-</sup>), and the surface hydroxyl (OH<sup>-</sup>) peak is not

obvious. The peaks of Ag@SnO<sub>2</sub>/TiO<sub>2</sub> at 529.3 and 530.6 eV correspond to lattice oxygen (O<sup>2-</sup>) and surface hydroxyl (OH<sup>-</sup>) [34,36]. It can be observed from Figure 4d that Ag 3d shows two characteristic peaks at 366.6 and 372.6 eV corresponding to Ag 3d<sub>5/2</sub> and Ag 3d<sub>3/2</sub>, respectively, indicating that the Ag element is in a zero-valent state [38,39]. Sn 3d (Figure 4e) exhibits two characteristic peaks at 486.5 and 494.9 eV, corresponding to Sn 3d<sub>5/2</sub> and Sn 3d<sub>3/2</sub>, respectively, implying that Sn element is in a +4 state [34].

### 3.4. PL Analysis

When photo-induced electron-hole pairs recombine, their excess energy will be released in the form of light, which can be responsible for the photoluminescence spectra [40,41]. Figure 5 shows the PL spectra of samples. The PL peak intensity of Ag@TiO<sub>2</sub> is lower than that of pure TiO<sub>2</sub>, indicating that Ag decoration inhibits the recombination of photogenerated electrons and holes. As the Fermi energy level of Ag particles is lower than the conduction band position of TiO<sub>2</sub>, the photogenerated electrons on the conduction band of TiO<sub>2</sub> will migrate to the surface of Ag particles, reducing the probability of recombination with holes in the valence band [42].

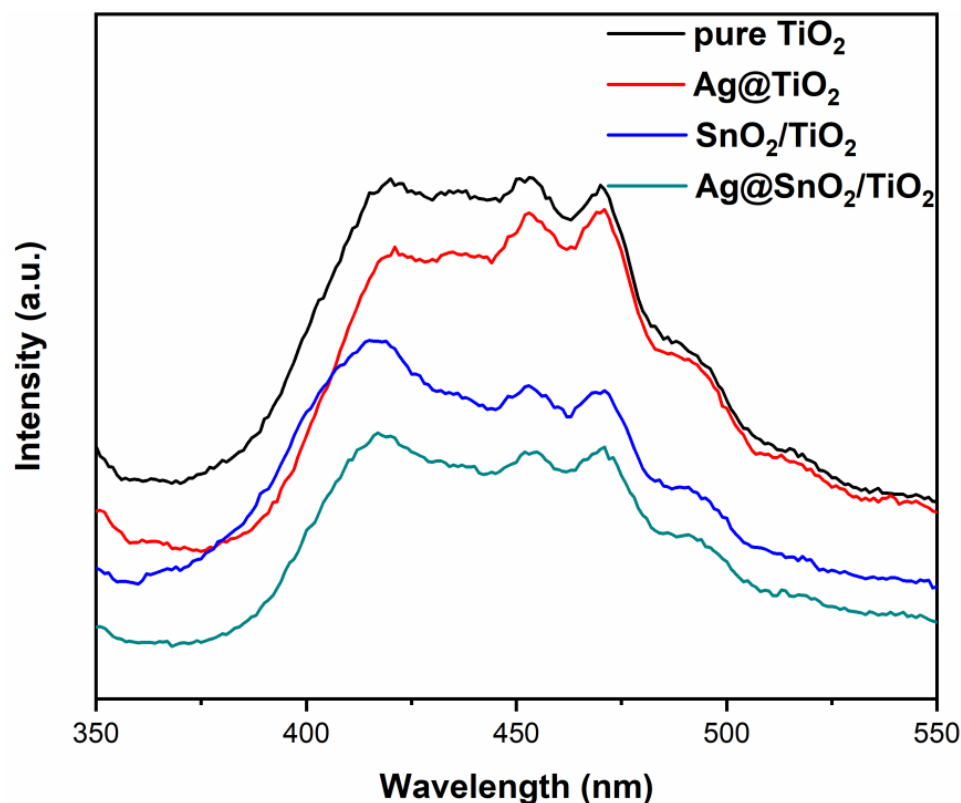


**Figure 5.** PL spectra of pure TiO<sub>2</sub>, Ag@TiO<sub>2</sub>, SnO<sub>2</sub>/TiO<sub>2</sub> and Ag@SnO<sub>2</sub>/TiO<sub>2</sub>.

SnO<sub>2</sub>/TiO<sub>2</sub> shows less PL peak intensity compared with pure TiO<sub>2</sub>, which implies that the recombination of photogenerated charges is suppressed by SnO<sub>2</sub> coupling. The electrons and holes transfer rapidly at the two-phase interface, which favors the photogenerated charge separation [43]. Remarkably, the PL peak intensity of Ag@SnO<sub>2</sub>/TiO<sub>2</sub> is the lowest, which means that Ag decoration and SnO<sub>2</sub> coupling produce a synergistic effect advancing the photogenerated charge separation. After Ag decoration and SnO<sub>2</sub> coupling modification, the utilization of photogenerated charges is enhanced significantly, which is beneficial to the photocatalytic activity [44].

### 3.5. DRS Analysis

The UV-visible absorption spectra of samples are shown in Figure 6. All samples show strong absorption in the ultraviolet region. After Ag decoration and SnO<sub>2</sub> coupling, the absorption edge does not change, indicating that the modification by Ag and SnO<sub>2</sub> has little effect on the band gap of TiO<sub>2</sub>. The absorption merely slightly increases in the 400–600 nm region after modification.

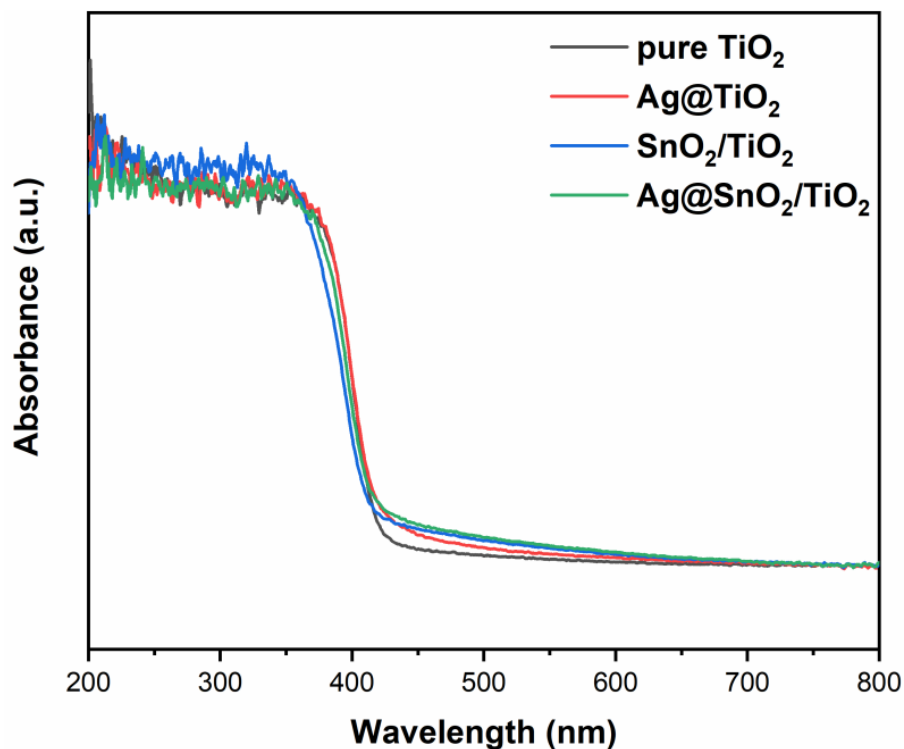


Figure 6. DRS spectra of pure TiO<sub>2</sub>, Ag@TiO<sub>2</sub>, SnO<sub>2</sub>/TiO<sub>2</sub> and Ag@SnO<sub>2</sub>/TiO<sub>2</sub>.

### 3.6. BET Analysis

Figure 7 shows the nitrogen adsorption-desorption isotherms and their corresponding pore size distribution curves of pure TiO<sub>2</sub> (a) and Ag@SnO<sub>2</sub>/TiO<sub>2</sub> (b). Both the two samples display type IV adsorption isotherm, showing mesoporous structure [45,46]. The pore size distribution of pure TiO<sub>2</sub> is between 5 and 20 nm, and the specific surface area is 39.7 m<sup>2</sup>/g. The pore size distribution of Ag@SnO<sub>2</sub>/TiO<sub>2</sub> is between 5 and 30 nm, and the specific surface area is 50.5 m<sup>2</sup>/g.

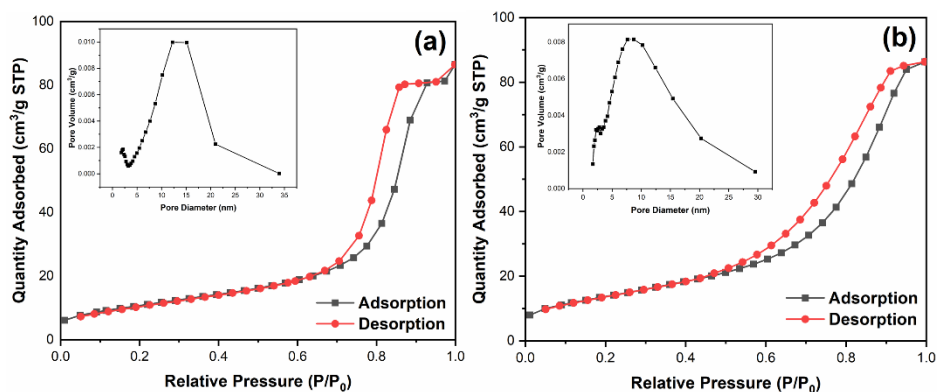


Figure 7. Nitrogen adsorption–desorption isotherms and the corresponding pore size distribution curves of pure TiO<sub>2</sub> (a) and Ag@SnO<sub>2</sub>/TiO<sub>2</sub> (b).

It can be seen from XRD that, after the addition of Ag or SnO<sub>2</sub>, the peak intensity decreases, and the half height width increases, indicating that the grain size is reduced, which is beneficial to obtain a higher specific surface area. [47–49]. The increased BET surface area indicates that Ag decoration and SnO<sub>2</sub> coupling modification enhances the specific surface area of anatase/rutile mixed crystal TiO<sub>2</sub>, which contributes to more reactive sites and higher photocatalytic efficiency [50].

### 3.7. Photocatalytic Activity

The photocatalytic performance of samples is evaluated by the degradation of TC, and the results are shown in Figure 8. After 30 min of reaction, the degradation degree of pure TiO<sub>2</sub> is 63.3%. The degradation degrees are improved by modification. The degradation degrees of Ag@TiO<sub>2</sub>, SnO<sub>2</sub>/TiO<sub>2</sub> and Ag@SnO<sub>2</sub>/TiO<sub>2</sub> are 78.4, 71.2 and 83.1%, respectively. Ag@SnO<sub>2</sub>/TiO<sub>2</sub> shows the highest photocatalytic activity. The kinetic curves of photocatalytic degradation towards TC are shown in Figure 8b. It can be observed that time *t* and  $-\ln(C/C_0)$  presents a linear relationship, and the photolysis reaction conforms to the first-order reaction [14]. The reaction rate constants of pure TiO<sub>2</sub>, Ag@TiO<sub>2</sub>, SnO<sub>2</sub>/TiO<sub>2</sub> and Ag@SnO<sub>2</sub>/TiO<sub>2</sub> are 0.034, 0.050, 0.041 and 0.057 min<sup>-1</sup>, respectively.

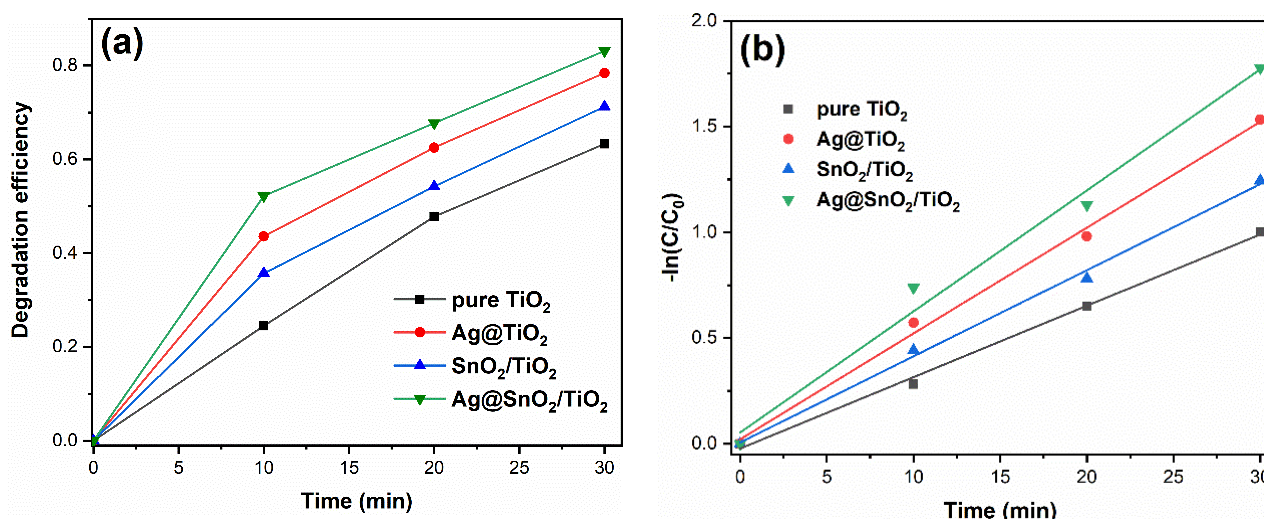


Figure 8. Degradation curves (a) and the kinetic curves of samples (b).

Ag decoration and SnO<sub>2</sub> coupling are beneficial to the separation of photogenerated charges and quantum efficiency, which has been proven by PL spectra. When Ag decoration and SnO<sub>2</sub> coupling are implemented simultaneously, a synergistic effect on suppressing the recombination of photogenerated electrons and holes is yielded. Therefore, Ag@SnO<sub>2</sub>/TiO<sub>2</sub> shows the lowest PL peak intensity, exhibiting the highest photocatalytic activity.

To determine the active species in photocatalytic reaction process, benzoquinone (BQ), ammonium oxalate (AO) and isopropanol (IPA) were added to capture the active groups, such as  $\cdot\text{O}_2^-$ ,  $\text{h}^+$  and  $\cdot\text{OH}$ , during the TC photodegradation process by Ag@SnO<sub>2</sub>/TiO<sub>2</sub> [51,52]. The results are shown in Figure 9. The degradation degree declines from 82.3 to 10.5% after adding BQ. The clearly decreased degradation degree indicates that  $\cdot\text{O}_2^-$  radicals are the main active groups. The degradation degrees are 40.9 and 67.9% after adding AO and IPA, separately, implying that the holes and  $\cdot\text{OH}$  radicals play secondary roles in the degradation process.

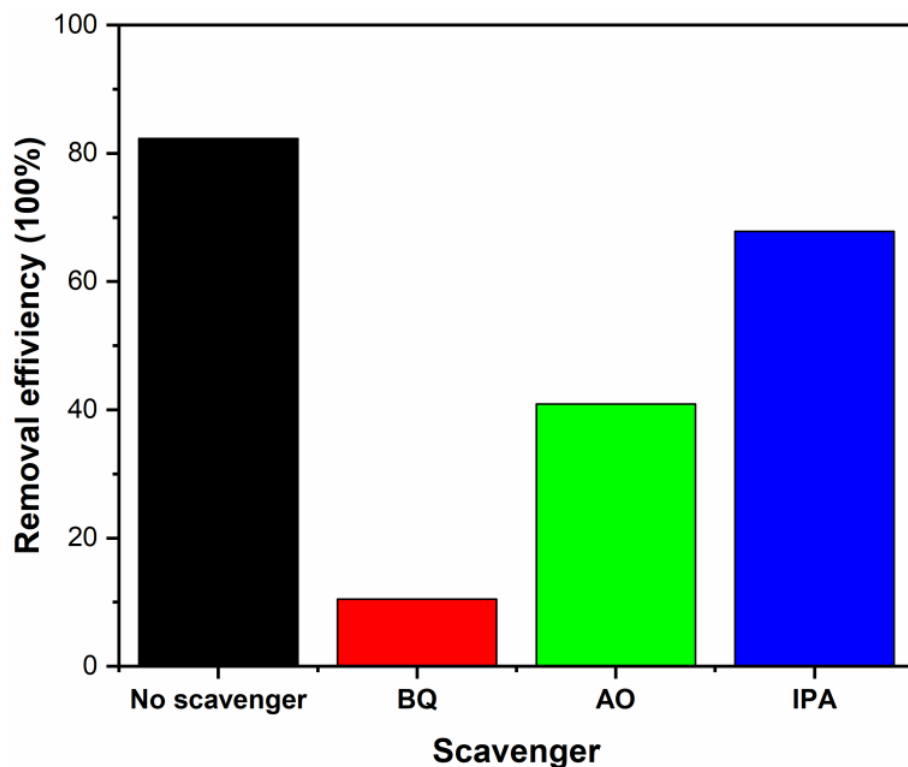


Figure 9. Degradation degrees of Ag@SnO<sub>2</sub>/TiO<sub>2</sub> with different capture agents.

### 3.8. The Degradation Mechanism

The energy band structure and the diagram of photogenerated charges transfer of Ag@SnO<sub>2</sub>/TiO<sub>2</sub> are shown in Figure 10. When electrons are excited by photons, they will jump from the valence band to the conduction band, thus, generating photo-induced electrons. Since the conduction band and valence band of anatase and rutile are higher than SnO<sub>2</sub>, the photogenerated electrons in anatase and rutile will migrate to the conduction band of SnO<sub>2</sub>, and the holes in the valence band of SnO<sub>2</sub> will transfer to the valence band of anatase and rutile.

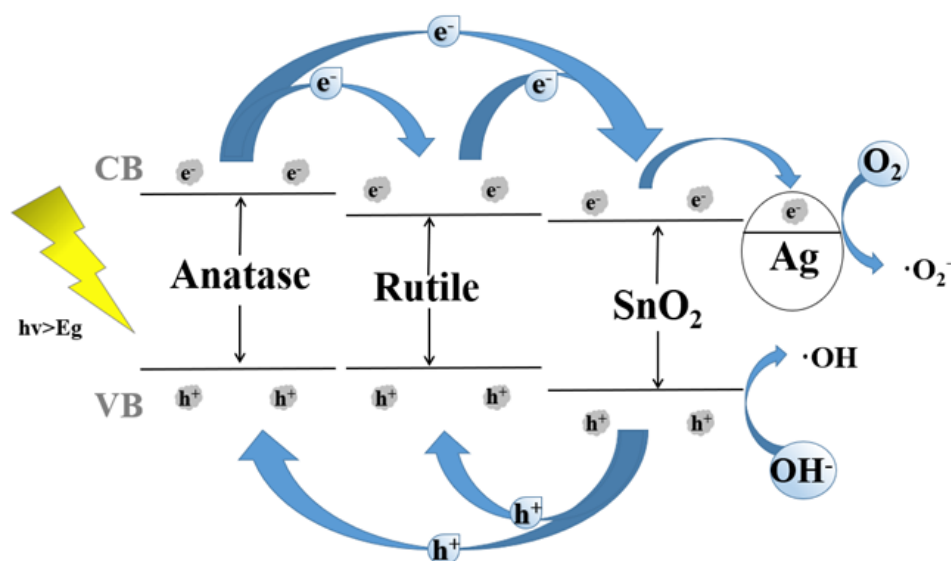
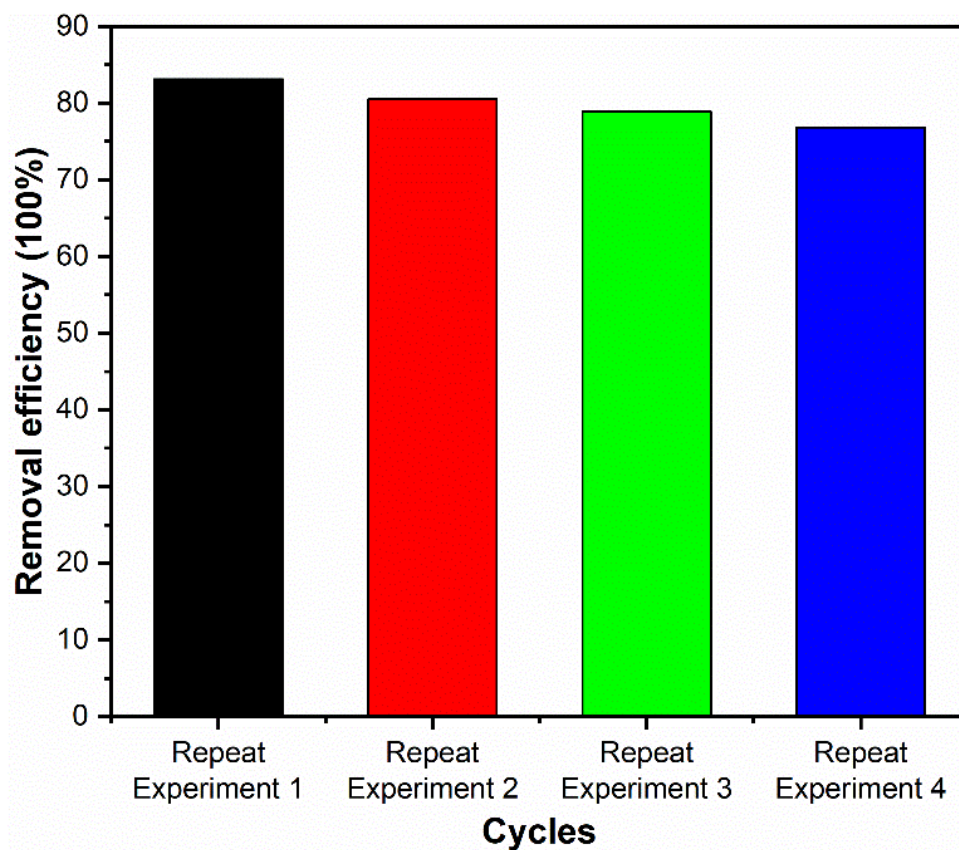


Figure 10. The energy band structure and the diagram of photogenerated charges transfer of Ag@SnO<sub>2</sub>/TiO<sub>2</sub>.

The SnO<sub>2</sub>/anatase/rutile three-phase coexistence structure is beneficial to accelerating the photogenerated charges transfer, improving the quantum utilization [42,53]. Moreover, when Ag particles deposit on the surface of SnO<sub>2</sub>/anatase/rutile, the photogenerated electrons will migrate to the surface of Ag particles, further advancing the separation of photo-induced charges [54,55]. The rapid transfer of photogenerated charges at the interfaces of Ag@SnO<sub>2</sub>/anatase/rutile composites is conducive to the formation of more radicals and the improvement of the photocatalytic efficiency [34].

The results of the cyclability of photocatalyst for TC degradation are shown in Figure 11. As the number of cycles increases, the degradation degree of TC decreases marginally. After four cycles, the degradation degree of TC by the Ag@SnO<sub>2</sub>/TiO<sub>2</sub> composite photocatalyst decreases from 83.1 to 76.8%. The slight decrease in the degradation degree indicates that the composite photocatalyst shows relatively high reusability.



**Figure 11.** The cyclability of the Ag@SnO<sub>2</sub>/TiO<sub>2</sub> photocatalyst for TC degradation.

The XRD pattern of the Ag@SnO<sub>2</sub>/TiO<sub>2</sub> composite photocatalyst after four cycles is shown in Figure 12. Compared with the initial sample, the positions of the diffraction peak do not change; however, the peak intensity decreases slightly. During the photocatalytic experiment, a very small amount of undegraded TC molecules may remain on the surface of photocatalyst, which decreases the diffraction peak intensity. On the other hand, the undegraded TC molecules occupy the active sites, resulting in a weak photocatalytic activity decrease [52,56,57]. This is also consistent with the repeated use experimental results.

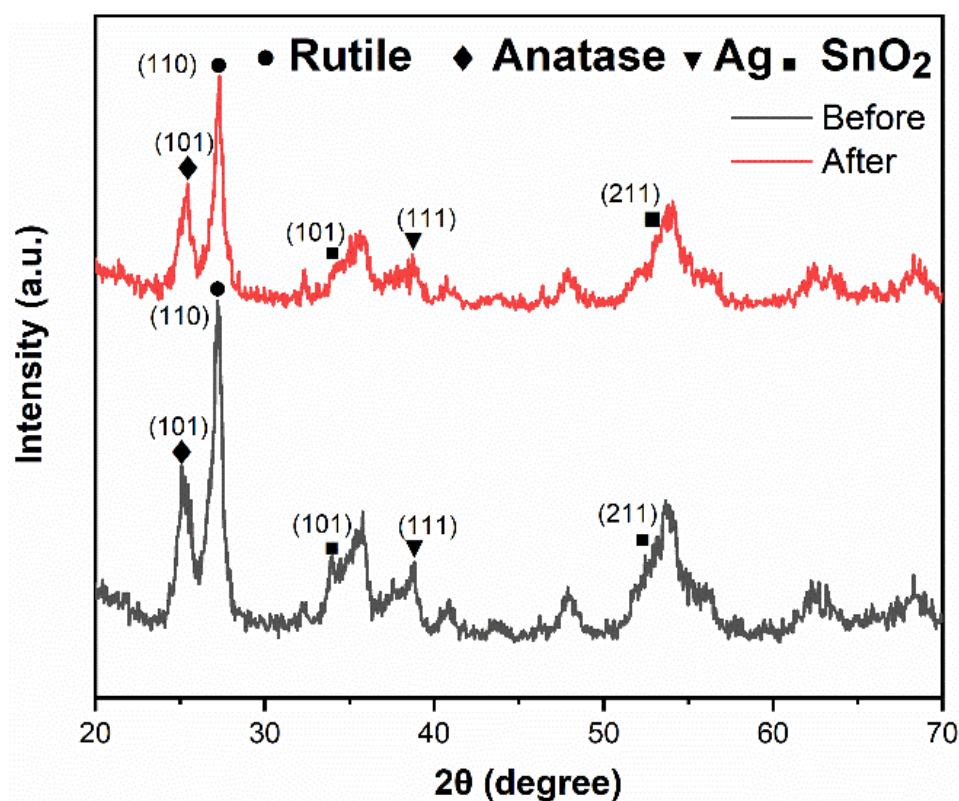


Figure 12. XRD patterns of Ag@SnO<sub>2</sub>/TiO<sub>2</sub> photocatalyst before and after the photocatalytic experiment.

#### 4. Conclusions

We prepared anatase/rutile mixed crystal TiO<sub>2</sub>, Ag@TiO<sub>2</sub>, SnO<sub>2</sub>/TiO<sub>2</sub>, Ag decoration and SnO<sub>2</sub> coupling modified TiO<sub>2</sub> and constructed a Ag@SnO<sub>2</sub>/TiO<sub>2</sub> composite photocatalytic material. XRD, SEM, TEM, XPS, PL, DRS and BET characterization and photocatalysis experiments were carried out on the samples. Ag exists in the form of 0 valence and Sn in the form of +4 valence. The results of the photocatalysis experiments showed that Ag decoration and SnO<sub>2</sub> coupling enhanced the performance of anatase/rutile mixed crystal TiO<sub>2</sub>.

When Ag decoration and SnO<sub>2</sub> coupling modification were implemented simultaneously, they had a synergistic effect on improving the charge separation and specific surface area, thus, exhibiting the highest photocatalytic activity. The first order reaction rate constant  $k$  of Ag@SnO<sub>2</sub>/TiO<sub>2</sub> sample was 0.057 min<sup>-1</sup>, which was 1.7-times higher than that of pure TiO<sub>2</sub> (0.034 min<sup>-1</sup>).

**Author Contributions:** Methodology, M.T., X.Z. and W.Z.; investigation, Y.X., D.Y. and S.L.; supervision, X.Z. and W.Z.; project administration, R.T. and X.Z.; formal analysis, M.T. and X.Z.; funding acquisition, M.T. and X.Z. All authors have read and agreed to the published version of the manuscript.

**Funding:** This research was funded by the Open Research Subject of Powder Metallurgy Engineering Technology Research Center of Sichuan Province (grant number SC-FMYJ2021-03), the Open Fund of Meat Processing Key Lab of Sichuan Province (grant number 21-R-21), the Open Project of Key Laboratory of Coarse Grain Processing, Ministry of Agriculture and Rural Affairs of China (2021HBZ001) and the Training Program for Innovation of Chengdu University (CDUCX2022006, S202011079053, CDU-CX-2021527).

**Institutional Review Board Statement:** Not applicable.

**Informed Consent Statement:** Not applicable.

**Data Availability Statement:** Data is contained within the article.

**Conflicts of Interest:** The authors declare that they have no conflict of interest.

## References

1. Wang, K.; Li, Y.; Zhang, G.K.; Li, J.; Wu, X.Y. 0D Bi nanodots/2D Bi<sub>3</sub>NbO<sub>7</sub> nanosheets heterojunctions for efficient visible light photocatalytic degradation of antibiotics: Enhanced molecular oxygen activation and mechanism insight. *Appl. Catal. B Environ.* **2018**, *240*, 39–49. [[CrossRef](#)]
2. Li, S.J.; Wang, C.C.; Liu, Y.P.; Xue, B.; Jiang, W.; Liu, Y.; Mo, L.Y.; Chen, X.B. Photocatalytic degradation of antibiotics using a novel Ag/Ag<sub>2</sub>S/Bi<sub>2</sub>MoO<sub>6</sub> plasmonic p-n heterojunction photocatalyst: Mineralization activity, degradation pathways and boosted charge separation mechanism. *Chem. Eng. J.* **2021**, *415*, 12899. [[CrossRef](#)]
3. Hajipour, P.; Eslami, A.; Bahrami, A.; Hosseini-Abari, A.; Saber, F.Y.; Mohammadi, R.; Mehr, M.Y. Surface modification of TiO<sub>2</sub> nanoparticles with CuO for visible-light antibacterial applications and photocatalytic degradation of antibiotics. *Ceram. Int.* **2021**, *47*, 33875–33885. [[CrossRef](#)]
4. Kuppasamy, S.; Kakarla, D.; Venkateswarlu, K.; Megharaj, M.; Yoon, Y.E.; Lee, Y.B. Veterinary antibiotics (VAs) contamination as a global agro-ecological issue: A critical view. *Agric. Ecosyst. Environ.* **2018**, *257*, 47–59. [[CrossRef](#)]
5. He, D.; Sun, Y.B.; Xin, L.; Feng, J.W. Aqueous tetracycline degradation by non-thermal plasma combined with nano-TiO<sub>2</sub>. *Chem. Eng. J.* **2014**, *258*, 18–25. [[CrossRef](#)]
6. Li, Y.H.; Liu, L.F.; Yang, F.L. Destruction of tetracycline hydrochloride antibiotics by FeOOH/TiO<sub>2</sub> granular activated carbon as expanded cathode in low-cost MBR/MFC coupled system. *J. Membr. Sci.* **2017**, *525*, 202–209. [[CrossRef](#)]
7. Wang, W.; Fang, J.J.; Shao, S.F.; Lai, M.; Lu, C.H. Compact and uniform TiO<sub>2</sub>@g-C<sub>3</sub>N<sub>4</sub> core-shell quantum heterojunction for photocatalytic degradation of tetracycline antibiotics. *Appl. Catal. B.* **2017**, *217*, 57–64. [[CrossRef](#)]
8. Shayegan, Z.; Lee, C.S.; Haghighat, F. TiO<sub>2</sub> photocatalyst for removal of volatile organic compounds in gas phase—A review. *Chem. Eng. J.* **2018**, *334*, 2408–2439. [[CrossRef](#)]
9. Nur, Y.; Lead, J.R.; Baalousha, M. Evaluation of charge and agglomeration behavior of TiO<sub>2</sub> nanoparticles in ecotoxicological media. *Sci. Total Environ.* **2015**, *535*, 45–53. [[CrossRef](#)]
10. Middepogu, A.; Hou, J.; Gao, X.; Lin, D.H. Effect and mechanism of TiO<sub>2</sub> nanoparticles on the photosynthesis of *Chlorella pyrenoidosa*. *Ecotoxicol. Environ. Saf.* **2018**, *161*, 497–506. [[CrossRef](#)]
11. Vinesh, V.; Shaheer, A.R.M.; Neppolian, B. Reduced graphene oxide (rGO) supported electron deficient B-doped TiO<sub>2</sub> (Au/B-TiO<sub>2</sub>/rGO) nanocomposite: An efficient visible light sonophotocatalyst for the degradation of Tetracycline (TC). *Ultrason. Sonochem.* **2019**, *50*, 302–310. [[CrossRef](#)] [[PubMed](#)]
12. Bahruji, H.; Bowker, M.; Davies, P.R.; Kennedy, J.; Morgan, D.J. The importance of metal reducibility for the photo-reforming of methanol on transition metal-TiO<sub>2</sub> photocatalysts and the use of non-precious metals. *Int. J. Hydrog. Energy* **2015**, *40*, 1465–1471. [[CrossRef](#)]
13. Tian, F.; Zhu, R.S.; Ouyang, F. Synergistic photocatalytic degradation of pyridine using precious metal supported TiO<sub>2</sub> with KBrO<sub>3</sub>. *J. Environ. Sci.* **2013**, *25*, 2299–2305. [[CrossRef](#)]
14. Zhang, Y.; Wang, T.; Zhou, M.; Wang, Y.; Zhang, Z.M. Hydrothermal preparation of Ag-TiO<sub>2</sub> nanostructures with exposed {001}/{101} facets for enhancing visible light photocatalytic activity. *Ceram. Int.* **2017**, *43*, 3118–3126. [[CrossRef](#)]
15. Li, H.; Shen, L.; Zhang, K.; Sun, B.; Ren, L.; Qiao, P.; Pan, K.; Wang, L.; Zhou, W. Surface plasmon resonance-enhanced solar-driven photocatalytic performance from Ag nanoparticle-decorated self-floating porous black TiO<sub>2</sub> foams. *Appl. Catal. B Environ.* **2018**, *220*, 111–117. [[CrossRef](#)]
16. Stucchi, M.; Bianchi, C.L.; Argiris, C.; Pifferi, V.; Neppolian, B.; Cerrato, G.; Boffito, D.C. Ultrasound assisted synthesis of Ag-decorated TiO<sub>2</sub> active in visible light. *Ultrason. Sonochem.* **2018**, *40*, 282–288. [[CrossRef](#)] [[PubMed](#)]
17. Ali, T.; Ahmed, A.; Alam, U.; Uddin, I.; Tripathi, P.; Muneer, M. Enhanced photocatalytic and antibacterial activities of Ag-doped TiO<sub>2</sub> nanoparticles under visible light. *Mater. Chem. Phys.* **2018**, *212*, 325–335. [[CrossRef](#)]
18. Kong, J.H.; Song, C.X.; Zhang, W.; Xing, Y.H.; Wan, M.; Wang, Y.Q. Enhanced visible-light-active photocatalytic performances on Ag nanoparticles sensitized TiO<sub>2</sub> nanotube arrays. *Superlattice. Microst.* **2017**, *109*, 579–587. [[CrossRef](#)]
19. Odling, G.; Robertson, N. BiVO<sub>4</sub>-TiO<sub>2</sub> Composite Photocatalysts for Dye Degradation Formed Using the SILAR Method. *ChemPhysChem* **2016**, *17*, 2872–2880. [[CrossRef](#)]
20. Golestanbagh, M.; Parvini, M.; Pendashteh, A. Preparation, Characterization and Photocatalytic Properties of Visible-Light-Driven CuO/SnO<sub>2</sub>/TiO<sub>2</sub> Photocatalyst. *Catal. Lett.* **2018**, *148*, 2162–2178. [[CrossRef](#)]
21. Guo, X.L.; Wan, J.F.; Yu, X.J.; Lin, Y.H. Study on preparation of SnO<sub>2</sub>-TiO<sub>2</sub>/Nano-graphite composite anode and electro-catalytic degradation of ceftriaxone sodium. *Chemosphere* **2016**, *164*, 421–429. [[CrossRef](#)]
22. Xun, H.T.; Zhang, Z.B.; Yu, A.H.; Yi, J.X. Remarkably enhanced hydrogen sensing of highly-ordered SnO<sub>2</sub>-decorated TiO<sub>2</sub> nanotubes. *Sens. Actuators B Chem.* **2018**, *273*, 983–990. [[CrossRef](#)]
23. De Mendonça, V.R.; Waldir, A.; Arenal, R.; Ribeiro, C. A building blocks strategy for preparing photocatalytically active anatase TiO<sub>2</sub>/rutile SnO<sub>2</sub> heterostructures by hydrothermal annealing. *J Colloid Interf. Sci.* **2017**, *505*, 454–459. [[CrossRef](#)]
24. Hu, W.Y.; Dong, F.Q.; Zhang, J.; Liu, M.X.; He, H.C.; Yang, D.M.; Deng, H.Q. A high-efficiency photocatalyst, flaky anatase@natural rutile composite using one-step microwave hydrothermal synthesis. *Res. Chem. Intermed.* **2018**, *44*, 705–720. [[CrossRef](#)]

25. Kampouri, S.; Ireland, C.P.; Valizadeh, B.; Oveisi, E.; Schouwink, P.; Mensi, M.; Stylianou, K.C. Mixed-phase MOF-derived Titanium Dioxide for Photocatalytic Hydrogen Evolution: The Impact of the Templated Morphology. *ACS Appl. Energy Mater.* **2018**, *1*, 6541–6548. [[CrossRef](#)]
26. Scotti, R.; D'Arienzo, M.; Testino, A.; Morazzoni, F. Photocatalytic mineralization of phenol catalyzed by pure and mixed phase hydrothermal titanium dioxide. *Appl. Catal. B Environ.* **2009**, *88*, 497–504. [[CrossRef](#)]
27. Lei, Y.C.; Yang, Y.; Zhang, P.L.; Zhou, J.J.; Wu, J.; Li, K.; Wang, W.W.; Chen, L.Y. Controllable One-Step Synthesis of Mixed-Phase TiO<sub>2</sub> Nanocrystals with Equivalent Anatase/Rutile Ratio for Enhanced Photocatalytic Performance. *Nanomaterials* **2021**, *11*, 1347. [[CrossRef](#)]
28. Fu, W.; Li, G.; Wang, Y.; Zeng, S.; Yan, Z.; Wang, J.; Xin, S.; Zhang, L.; Wu, S.; Zhang, Z. Facile formation of mesoporous structured mixed-phase (anatase/rutile) TiO<sub>2</sub> with enhanced visible light photocatalytic activity. *Chem. Commun.* **2017**, *54*, 58–61. [[CrossRef](#)]
29. Cheng, H.; Ye, J.; Sun, Y.; Yuan, W.; Tian, J.; Bogale, R.F.; Tian, P.; Ning, G. Template-induced synthesis and superior antibacterial activity of hierarchical Ag/TiO<sub>2</sub> composites. *RSC Adv.* **2015**, *5*, 80668. [[CrossRef](#)]
30. Khojasteh, F.; Mersagh, M.R.; Hashemipour, H. The influences of Ni, Ag-doped TiO<sub>2</sub> and SnO<sub>2</sub>, Ag-doped SnO<sub>2</sub>/TiO<sub>2</sub> nanocomposites on recombination reduction in dye synthesized solar cells. *J. Alloys Compd.* **2021**, *890*, 161709. [[CrossRef](#)]
31. Nakajima, T.; Nakamura, T.; Tsuchiya, T. Crystal-Plane Dependence of Nb-Doped Rutile TiO<sub>2</sub> Single Crystals on Photoelectrochemical Water Splitting. *Catalysts* **2019**, *9*, 725. [[CrossRef](#)]
32. De, D.S.; Behara, D.K.; Saha, S.; Kumar, A.; Subramaniam, A.; Sivakumar, S.; Pala, R.G.S. Design of iso-material heterostructures of TiO<sub>2</sub> via seed mediated growth and arrested phase transitions. *Phys. Chem. Chem. Phys.* **2020**, *22*, 25366. [[CrossRef](#)] [[PubMed](#)]
33. Yu, Y.; Zhang, Y.; Zou, K.; Chen, G.; Zhang, Y.; Li, H.; Lu, Y.; Zhang, Q.; He, Y.B. High energy density and efficiency in (Pb,La)(Zr,Sn,Ti)O<sub>3</sub> antiferroelectric ceramics with high La<sup>3+</sup> content and optimized Sn<sup>4+</sup> content. *Ceram. Int.* **2019**, *45*, 24419–24424. [[CrossRef](#)]
34. Jia, C.; Chen, H.-S.; Yang, P. Construction of hollow waxberry-like rutile-/anatase-TiO<sub>2</sub>/SnO<sub>2</sub> towards enhanced photocatalysis. *J. Ind. Eng. Chem.* **2018**, *58*, 278–289. [[CrossRef](#)]
35. Jia, C.; Dong, T.; Li, M.; Wang, P.; Yang, P. Preparation of anatase/rutile TiO<sub>2</sub>/SnO<sub>2</sub> hollow heterostructures for gas sensor. *J. Alloys Compd.* **2018**, *769*, 521–531. [[CrossRef](#)]
36. Zhang, Z.; Ma, Y.; Bu, X.; Wu, Q.; Hang, Z.; Dong, Z.; Wu, X. Facile one-step synthesis of TiO<sub>2</sub>/Ag/SnO<sub>2</sub> ternary heterostructures with enhanced visible light photocatalytic activity. *Sci. Rep.* **2018**, *8*, 10532. [[CrossRef](#)] [[PubMed](#)]
37. Liu, H.; Fan, H.; Wu, R.; Tian, L.; Yang, X.; Sun, Y. Nitrogen-doped black TiO<sub>2</sub> spheres with enhanced visible light photocatalytic performance. *SN Appl. Sci.* **2019**, *1*, 487. [[CrossRef](#)]
38. Sheng, J.; Tong, H.; Xu, H.; Tang, C. Preparation and photocatalytic activity of SnO<sub>2</sub>@TiO<sub>2</sub> core-shell composites modified by Ag. *Catal. Surv. Asia* **2016**, *20*, 167–172. [[CrossRef](#)]
39. Zhao, L.N.; Jia, Y.H.; You, H.; Wang, S.T.; Fu, L. Photocatalytic performance and application outlook of 3D TiO<sub>2</sub>/titanium mesh modified by GO-Ag joined-deposition. *Catal. Today* **2020**, *340*, 106–114. [[CrossRef](#)]
40. Žerjav, G.; Arshad, M.S.; Djinović, P.; Junkar, I.; Kovač, J.; Zavašnik, J.; Pintar, A. Improved electron-hole separation and migration in anatase TiO<sub>2</sub> nanorod/reduced graphene oxide composites and their significance on photocatalytic performance. *Nanoscale* **2017**, *9*, 4578–4592. [[CrossRef](#)]
41. Gao, Y.; Fang, P.; Chen, F.; Liu, Y.; Liu, Z.; Wang, D.; Dai, Y. Enhancement of stability of N-doped TiO<sub>2</sub> photocatalysts with Ag loading. *Appl. Surf. Sci.* **2013**, *265*, 796–801. [[CrossRef](#)]
42. Sun, B.; Chen, Y.; Tao, L.; Zhao, H.; Zhou, G.; Xia, Y.; Wang, H.; Zhao, Y. Nanorods array of SnO<sub>2</sub> quantum dots interspersed multiphase TiO<sub>2</sub> heterojunctions with highly photocatalytic water splitting and self-rechargeable battery-like applications. *ACS Appl. Mater. Inter.* **2019**, *11*, 2071–2081. [[CrossRef](#)] [[PubMed](#)]
43. Ye, J.; Xu, J.T.; Tian, D.; Zhao, X.; Wang, Q.; Wang, J.; Li, Y.; Zhao, C.; Liu, Z.; Fu, Y. Efficient photocatalytic reduction of CO<sub>2</sub> by a rhenium-doped TiO<sub>2-x</sub>/SnO<sub>2</sub> inverse opal S-scheme heterostructure assisted by the slow-phonon effect. *Sep. Purif. Technol.* **2021**, *277*, 119431. [[CrossRef](#)]
44. Jia, T.; Liu, M.; Zheng, C.; Long, F.; Min, Z.; Fu, F.; Yu, D.; Li, J.; Lee, J.H.; Kim, N.H. One-Pot Hydrothermal Synthesis of La-Doped ZnIn<sub>2</sub>S<sub>4</sub> Microspheres with Improved Visible-Light. *Nanomaterials* **2020**, *10*, 2026. [[CrossRef](#)]
45. Adyani, S.M.; Ghorbani, M. A comparative study of physicochemical and photocatalytic properties of visible light responsive Fe; Gd and P single and tri-doped TiO<sub>2</sub> nanomaterials. *J. Rare Earths* **2018**, *36*, 72–85. [[CrossRef](#)]
46. Lei, X.F.; Xue, X.X.; Yang, H. Preparation and characterization of Ag-doped TiO<sub>2</sub> nanomaterials and their photocatalytic reduction of Cr (VI) under visible light. *Appl. Surf. Sci.* **2014**, *321*, 396–403. [[CrossRef](#)]
47. Yu, J.; Yu, J.C.; Zhao, X.J. The Effect of SiO<sub>2</sub> Addition on the Grain Size and Photocatalytic Activity of TiO<sub>2</sub> Thin Films. *J. Sol-Gel Sci. Technol.* **2002**, *24*, 95–103. [[CrossRef](#)]
48. Chen, Y.; Liu, K.R. Fabrication of Ce/N co-doped TiO<sub>2</sub>/diatomite granule catalyst and its improved visible-light-driven photoactivity. *J. Hazard. Mater.* **2017**, *324*, 139–150. [[CrossRef](#)]
49. Sibin, C.P.; Kumar, S.R.; Mukundan, P.; Warriar, K.G.K. Structural modifications and associated properties of lanthanum oxide doped sol-gel nanosized titanium oxide. *Chem. Mater.* **2002**, *14*, 2876–2881. [[CrossRef](#)]
50. Wu, D.; Li, C.; Zhang, D.S.; Wang, L.L.; Zhang, X.; Shi, Z.; Lin, Q. Photocatalytic improvement of Y<sup>3+</sup> modified TiO<sub>2</sub> prepared by a ball milling method and application in shrimp wastewater treatment. *RSC Adv.* **2019**, *9*, 14609. [[CrossRef](#)]

51. Tang, M.; Xia, Y.; Yang, D.; Liu, J.; Zhu, X.; Tang, R. Effects of Hydrothermal Time on Structure and Photocatalytic Property of Titanium Dioxide for Degradation of Rhodamine B and Tetracycline Hydrochloride. *Materials* **2021**, *14*, 5674. [[CrossRef](#)]
52. Wang, Y.; Qiao, M.; Lv, J.; Xu, G.; Zheng, Z.; Zhang, X.; Wu, Y. g-C<sub>3</sub>N<sub>4</sub>/g-C<sub>3</sub>N<sub>4</sub> isotype heterojunction as an efficient platform for direct photodegradation of antibiotic. *Fuller. Nanotub. Carbon Nanostruct.* **2018**, *26*, 210–217. [[CrossRef](#)]
53. Zhu, X.; Zhu, R.; Pei, L.; Liu, H.; Xu, L.; Wang, J.; Feng, W.; Jiao, Y.; Zhang, W. Fabrication, characterization, and photocatalytic activity of anatase/rutile/SnO<sub>2</sub> nanocomposites. *J. Mater. Sci.* **2019**, *30*, 21210–21218. [[CrossRef](#)]
54. Zhang, Y.; Wang, L.; Yu, S.; Jiang, H.; Yun, Y.; Sun, Y.; Shi, J. Ag-induced synthesis of three dimensionally ordered macroporous anatase/rutile homojunction for solar light-driven Z-scheme photocatalysis. *Sol. Energy* **2018**, *174*, 770–779. [[CrossRef](#)]
55. Qin, J.; Wang, J.; Yang, J.; Hu, Y.; Fu, M.; Ye, D. Metal organic framework derivative-TiO<sub>2</sub> composite as efficient and durable photocatalyst for the degradation of toluene. *Appl. Catal. B Environ.* **2020**, *267*, 118667. [[CrossRef](#)]
56. Prakash, K.; Kumar, P.S.; Pandiaraj, S.; Saravanakumar, K.; Karuthapandian, S. Controllable synthesis of SnO<sub>2</sub> photocatalyst with superior photocatalytic activity for the degradation of methylene blue dye solution. *J. Exp. Nanosci.* **2021**, *11*, 1–18. [[CrossRef](#)]
57. Wu, D.; Guo, J.; Ge, Z.-H.; Feng, J. Facile Synthesis Bi<sub>2</sub>Te<sub>3</sub> based nanocomposites: Strategies for enhancing charge carrier separation to improve photocatalytic activity. *Nanomaterials* **2021**, *11*, 3390. [[CrossRef](#)]